

Influence of Silicon Content, Strain Rate and Temperature on Toughness and Strength of Solid Solution Strengthened Ferritic Ductile Cast Iron

Tomohiro Ikeda^{1,*}, Takuo Umetani¹, Nobuhiro Kai¹, Keisaku Ogi¹, Nao-Aki Noda² and Yoshikazu Sano²

¹Research & Development Center, HINODE, Ltd., Saga 849-0101, Japan

²Department of Mechanical and Control Engineering, Kyushu Institute of Technology, Fukuoka 804-8550, Japan

High Silicon Solid Solution Strengthened Ferritic Ductile Cast Iron possesses advantages, such as better combination of strength-elongation, higher fatigue strength, smaller section thickness sensitivity, higher machinability etc., over conventional ferrite-pearlite type ductile cast iron. However, industrial application of high Si ductile cast iron is still very limited, because of the lower Charpy impact value at room temperature. As the toughness of iron strongly depends on the strain rate as well as temperature, dynamic three-point bending tests are conducted on 3~4%Si ferritic ductile cast iron at stroke speed of 10^{-3} ~ 10^2 mm/s, and at -20 ~ 22°C . The relations of the crack initiation energy E_i , the crack propagation energy E_p , the total absorbed energy E_t and the maximum bending stress $\sigma_{b,max}$ to the strain rate show abrupt dropping of these characteristic values at critical strain rate, depending on silicon content and test temperature. $\sigma_{b,max}$ keeps increasing with increasing strain rate $\dot{\epsilon}$ as far as the fracture origin is ductile, it slightly decreases over $\dot{\epsilon}_\sigma = \dot{\epsilon}_{fD}$ where the dimple fracture completely disappears. $\sigma_{b,max}$, E_t and E_i of each silicon iron is well expressed in relation to strain rate-temperature parameter R , $T \ln(A/\dot{\epsilon})$. The critical R values for E_t , E_i , and $\sigma_{b,max}$ (R_t , R_i and R_σ) decrease linearly with decreasing the silicon content of iron. The critical value for $\sigma_{b,max}$ (R_σ) is lowest, indicating R_σ gives a wider design tolerance. [doi:10.2320/matertrans.F-M2016832]

(Received April 25, 2016; Accepted September 2, 2016; Published October 14, 2016)

Keywords: high silicon ductile cast iron, ferritic matrix, dynamic strength, toughness, strain rate, temperature

1. Introduction

In recent years, high silicon ductile cast iron containing 3.2 to 4.2%Si has been attracting attention as a new candidate for various mechanical and structural components¹⁻³). The three strength-elongation levels of high silicon ductile cast iron are already standardized in EN as "High Silicon Solid Solution Strengthened Ferritic Ductile Cast Iron"⁴). In this high silicon ductile cast iron, higher strength is obtained by increasing silicon addition, while the pearlite ratio should be controlled to attain the required strength in the conventional ferrite-pearlite type ductile cast iron. Although the elongation of high silicon ductile cast iron decreases with increasing silicon content, the elongation is higher than that of similar strength level of conventional ferrite-pearlite type ductile cast iron⁵).

As the mechanical properties of high silicon ductile cast iron are controlled mostly by silicon content and higher silicon strongly promotes stable solidification, this iron shows much smaller section thickness sensitivity especially in heavier castings. Furthermore, high silicon ductile cast iron possesses a better machinability, and hence a higher productivity, than the conventional ductile cast iron. Contrary to these advantages, high silicon ductile cast iron shows a brittle fracture near room temperature in Charpy impact test, since the ductile-brittle transition temperature rises with the increase in silicon content of ferritic matrix⁶⁻⁸). This should be a main reason why industrial application of high silicon ductile cast iron is still very limited.

However, Charpy impact test is sometimes not suitable for evaluating the impact strength for structural component design, because the impact speed does not correspond to the real products failure. The toughness of iron strongly depends on the strain rate as well as temperature, and ductile-brittle transition temperature of conventional ductile cast iron becomes

higher with the increase in strain rate^{9,10}). But, it is difficult to control the pendulum impact speed in Charpy impact test. Moreover, it should be noted that Charpy absorbed energy has not been directly used as design strength.

Therefore, a key objective of this study is investigating the influence of strain rate and temperature on toughness and strength of ferritic ductile cast iron containing from 3 to 4%Si. Using Charpy V-notch specimens, the three-point bending tests are conducted at stroke speed = 10^{-3} ~ 10^2 mm/s, and at -20 ~ 22°C . Based on obtained load-displacement curves, the absorbed energy in fracture process and the notch bending strength are determined. The results are discussed with the strain rate-temperature parameter.

2. Experimental Procedure

2.1 Test materials

With 300 kW high frequency electric furnace and a ladle, ductile cast iron melts containing from 3 to 4%Si were prepared by the Sandwich Method and cast into sand molds for JIS Type II Y-shaped blocks¹¹). Table 1 shows their chemical compositions. The silicon content was varied from 4.01% to 3.02%. The carbon content was also changed from 3.22 to 3.42% to keep the carbon equivalent about 4.4. All test samples were taken from the as cast blocks, as shown in Fig 1.

Figure 2 shows typical microstructures of as cast test samples. Apparently all samples have fully ferritic matrix. Ta-

Table 1 Chemical compositions of as cast samples.

Material	C	Si	Mn	P	S	Cu	Mg
4.0%Si	3.22	4.01	0.34	0.030	0.008	0.01	0.044
3.7%Si	3.20	3.72	0.32	0.020	0.008	0.02	0.044
3.3%Si	3.28	3.31	0.25	0.020	0.002	0.01	0.039
3.0%Si	3.42	3.02	0.32	0.030	0.004	0.01	0.043

*Corresponding author, E-mail: t_ikeda@hinosuid.co.jp

Table 2 shows microstructure characteristics and Brinell hardness of test samples based on the analysis according to JIS-G5502¹¹⁾, JIS-G 0551¹²⁾ and JIS-Z 2243 standard¹³⁾. Every sample has nearly the same microstructure characteristics, that is, nodule count, average nodule diameter, nodularity, graphite area fraction and ferrite grain size number. The Brinell hardness increase with increasing the silicon content.

Figure 3 shows the tensile properties of test samples. Tensile tests were made on JIS No.4 test piece with the diameter = 14 mm and the gage length = 50 mm according to JIS-Z 2241 standard¹⁴⁾. The tensile strength and the proof stress linearly increase and the elongation decreases with increasing

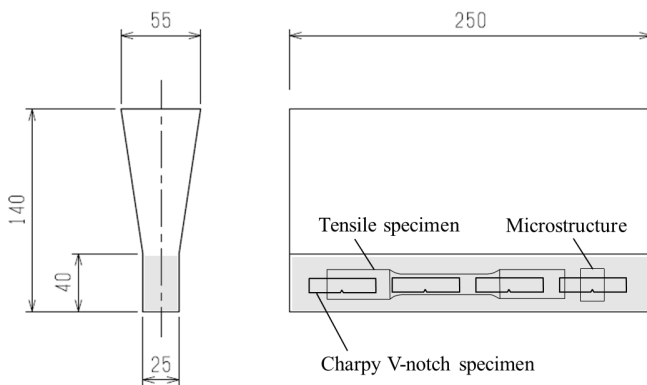


Fig. 1 Schematic view of Y-shaped block.

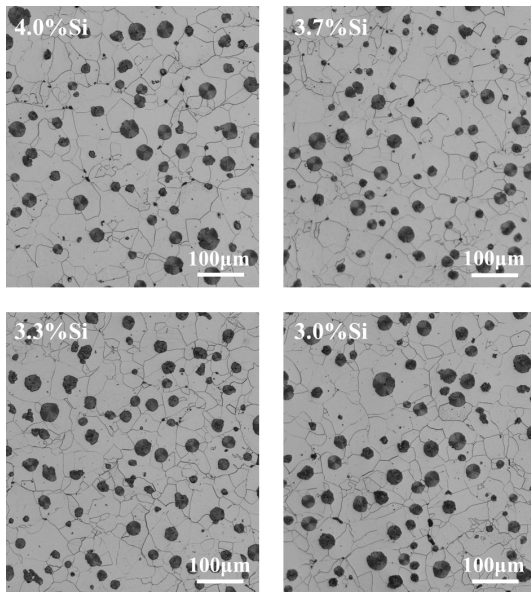


Fig. 2 Microstructures of as cast samples.

the silicon content. The small difference in Mn content in Table 1 and microstructure characteristics in Table 2 might give negligible effect on the tensile properties¹⁵⁾.

2.2 Dynamic three-point bending test

Dynamic three-point bending test was conducted on Charpy V-notch specimens shown in Fig. 4¹⁶⁾. The test was carried out in the range of stroke speed, $\nu = 10^{-3} \sim 10^2$ mm/s, at $-20 \sim 22^\circ\text{C}$ by using Electro hydraulic servo testing machine (Shimadzu: E100kN). The bending jig was prepared in the same shape and size as the Charpy impact testing machine, so that the span length L_s was 40 mm.

The strain rate $\dot{\epsilon}$ is calculated by using eq. (1)^{9,17-19)}, where h = test specimen width, $Q = 1.94^{9,17,18)}$, ν = stroke speed, L_s = span length.

$$\dot{\epsilon} = 6h\nu Q/L_s^2 \quad (1)$$

Maximum nominal bending stress $\sigma_{b,max}$ is calculated by eq. (2)^{20,21)}, where P_{max} = maximum load, b = test specimen thickness.

$$\sigma_{b,max} = 3P_{max}L_s/2bh^2 \quad (2)$$

Figure 5 shows a typical load-displacement curve by the three-point bending test. Absorbed energy in the fracture process is obtained as the area under the load-displacement curve. E_i is absorbed energy before maximum load. It was reported that the microcrack extends to the macrocrack larger than 0.1 mm at the vicinity of the maximum load, and then propagates²²⁾. Therefore, E_i is defined as the macroscopic crack initiation energy. E_p is absorbed energy after the maximum load, that is, the crack propagation energy. E_t is total

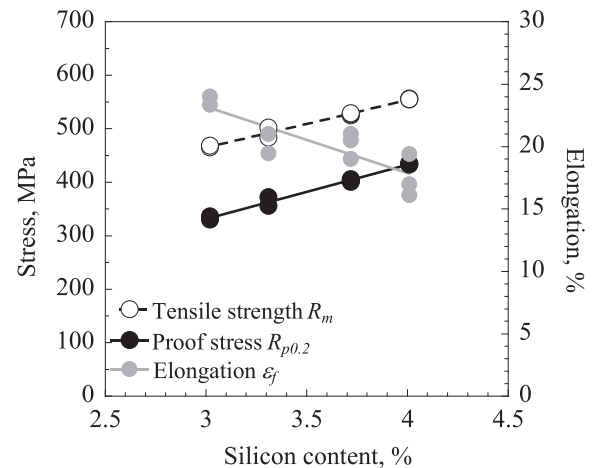


Fig. 3 Relationship between mechanical properties and silicon content.

Table 2 Microstructure characteristics and Brinell hardness of as cast samples.

Material	Nodule count mm^{-2}	Average nodule diameter, μm	Nodularity, %	Graphite area fraction, %	Pearlite ratio, %	Ferrite grain size number (JIS G 0551)	Brinell hardness
4.0%Si	208	26.7	91.5	10.5	0.0	8.0	182
3.7%Si	192	28.1	91.9	10.6	0.0	7.8	179
3.3%Si	202	27.3	90.2	10.2	0.0	8.0	171
3.0%Si	174	30.3	92.9	11.7	1.4	7.9	165

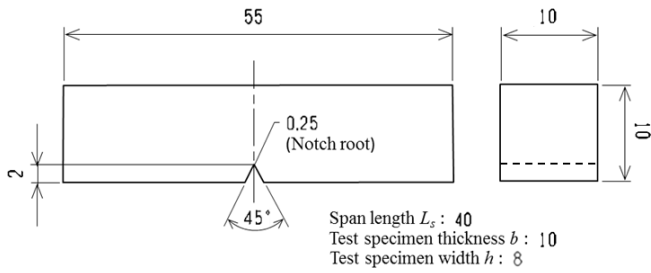


Fig. 4 Dimension of Charpy V-notch specimen.

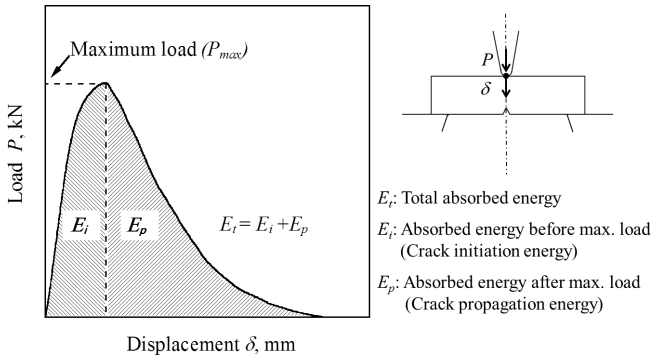


Fig. 5 Definition of absorbed energy on the three-point bending test.

absorbed energy, therefore $E_t = E_i + E_p$.

Fractographic analysis was made with an optical microscopy and Scanning Electron Microscopy (Hitachi S-3400N). The ductile fracture surface ratio f_D was evaluated as the ratio of the ductile fracture surface area to the total fracture surface area of the specimen from photomicrographs taken on the whole specimen surface at 20-fold magnification. SEM observation was also made to reveal the details of fracture morphology especially near V-notch root where the fracture started.

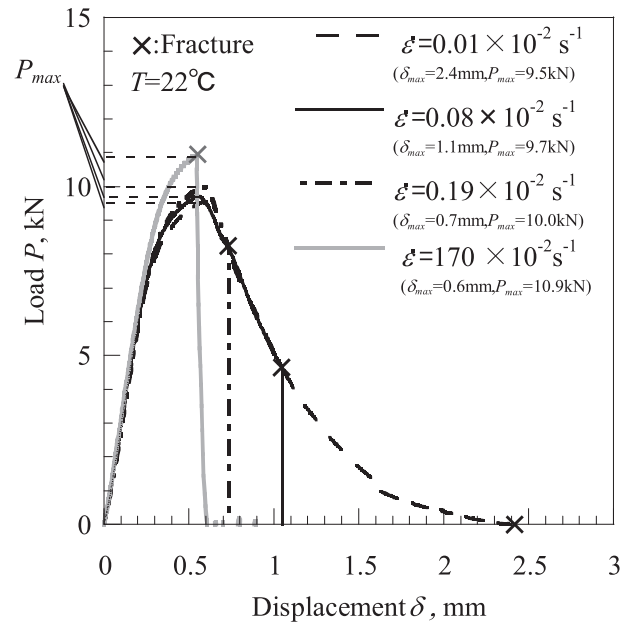
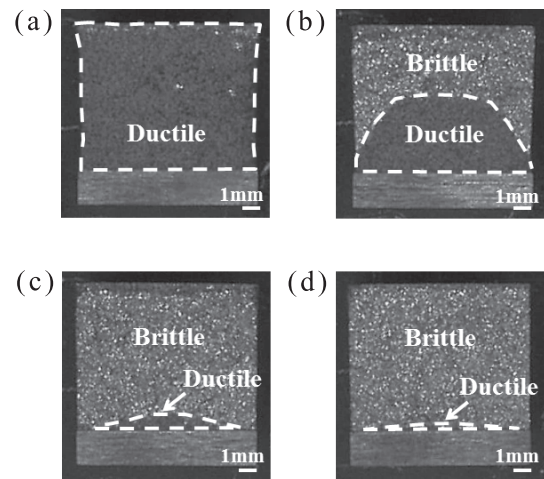
3. Results and Discussions

3.1 Dependency of absorbed energy and notch bending strength on strain rate at 22°C for 4%Si ductile cast iron

Figure 6 shows the load-displacement curves tested under various strain rates $\dot{\epsilon}$ at temperature $T = 22^\circ\text{C}$ for 4%Si iron. Obviously, with increasing $\dot{\epsilon}$ the maximum displacement δ_{max} and hence E_p were decreasing. On the other hand, the maximum load P_{max} slightly increases with increasing $\dot{\epsilon}$. This phenomenon might be similar to the increase in strength of iron and steel with increasing strain rate.

Figure 7 shows the fracture surface of tested specimens. The fracture surface is composed of black and white bright areas, and the black area significantly decreases with an increase in $\dot{\epsilon}$. The SEM images on both areas, shown in Fig. 8, reveals that black area is made of dimple patterns characterizing ductile fracture and the white area is cleavage fracture surface characterizing brittle fracture.

Based on the load-displacement curves in Fig. 6 and photographs in Fig. 7, E_t , E_p , E_i and ductile fracture surface ratio f_D are determined, and the results are given in relation to strain rate $\dot{\epsilon}$, as shown in Fig. 9. The crack propagation energy E_p and also the total absorbed energy E_t start dropping at critical

Fig. 6 Load-displacement curves tested under various $\dot{\epsilon}$ at $T = 22^\circ\text{C}$ for 4%Si iron.Fig. 7 Fracture surfaces tested at various $\dot{\epsilon}$ at $T = 22^\circ\text{C}$ for 4%Si iron. (a) $\dot{\epsilon} = 0.01 \times 10^{-2} \text{ s}^{-1}$, (b) $\dot{\epsilon} = 0.08 \times 10^{-2} \text{ s}^{-1}$, (c) $\dot{\epsilon} = 0.19 \times 10^{-2} \text{ s}^{-1}$, (d) $\dot{\epsilon} = 170 \times 10^{-2} \text{ s}^{-1}$.

strain rate $\dot{\epsilon}_p = 1.3 \times 10^{-3} \text{ s}^{-1}$, as indicated by the black arrow in the Fig. 9(a). As shown in Fig. 9(b), fully ductile fracture occurs below $\dot{\epsilon}_p$, and the ductile fracture surface ratio f_D starts dropping drastically at $\dot{\epsilon}_p$, thus the critical strain rate of f_D is in agreement with that of E_p . On the other hand, the macrocrack initiation energy E_i is almost unchanged even above $\dot{\epsilon}_p$, indicating the reduction of E_t is caused by the decrease in E_p .

And as explained above, the maximum nominal bending stress $\sigma_{b,max}$ tends to increase with increasing $\dot{\epsilon}$ as in Fig. 10. Figure 11 shows SEM image at the notch root in Fig. 7(d). Even though the photomicrograph shows almost no ductile fracture surface in Fig. 7(d), SEM images reveal that a slight amount of dimple patterns appear near the notch root. This slight amount of dimples should be caused by the initial stage of fracture. Several researchers examined the microcrack initiation at the notch root under three-point bending test^(22,23).

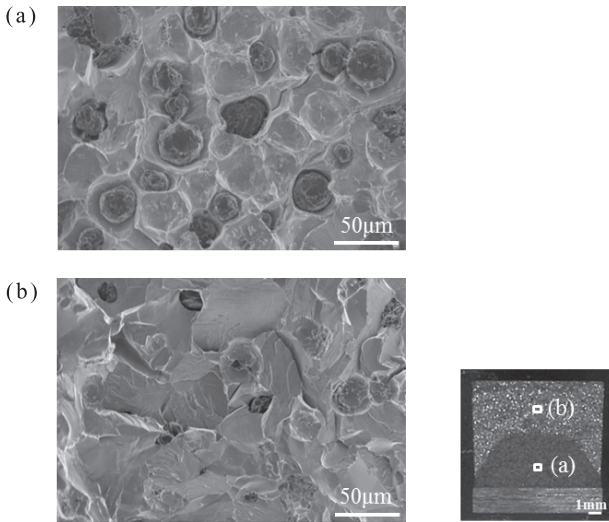


Fig. 8 SEM images of the black (ductile) area (a) and white (brittle) area (b) in Fig. 7(b).

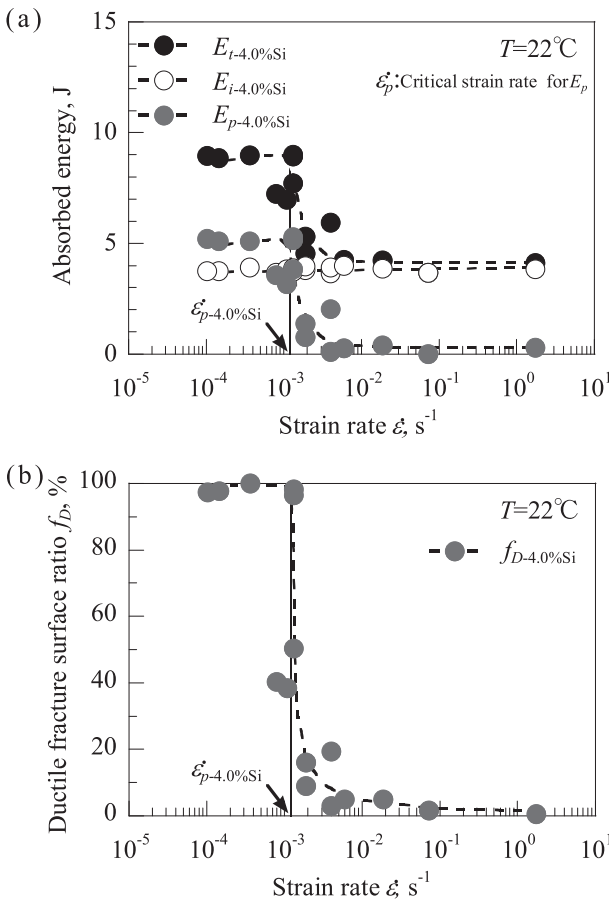


Fig. 9 Influence of the strain rate $\dot{\epsilon}$ on the absorbed energy (a) and ductile fracture surface ratio f_D (b) at temperature $T = 22^\circ\text{C}$ for 4% Si iron.

They reported that when ductile fracture occurs, an approximately $50 \mu\text{m}$ microcrack initiates at the notch root²²⁾. At the same time, separation of spheroidal graphite and ferritic matrix was confirmed²²⁾. Then, the microcrack extends to the macrocrack larger than 0.1 mm at the vicinity of the maximum load, and then propagates²³⁾. When brittle fracture occurs, a microcrack propagates rapidly almost at the same time of crack initiation²³⁾. Therefore, in Fig. 7(d), it is conjectured

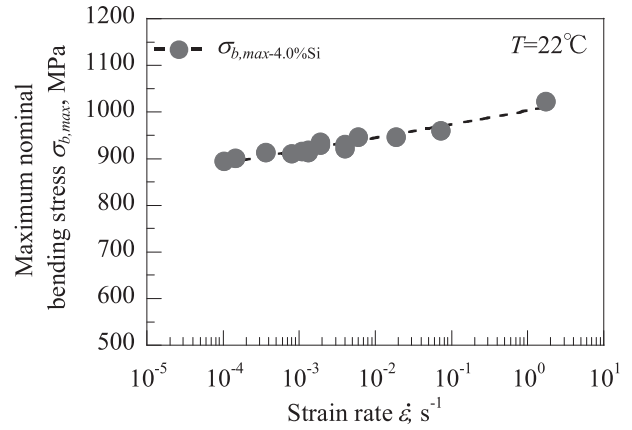


Fig. 10 Influence of $\dot{\epsilon}$ on maximum nominal bending stress $\sigma_{b,max}$ at $T = 22^\circ\text{C}$ for 4% Si iron.

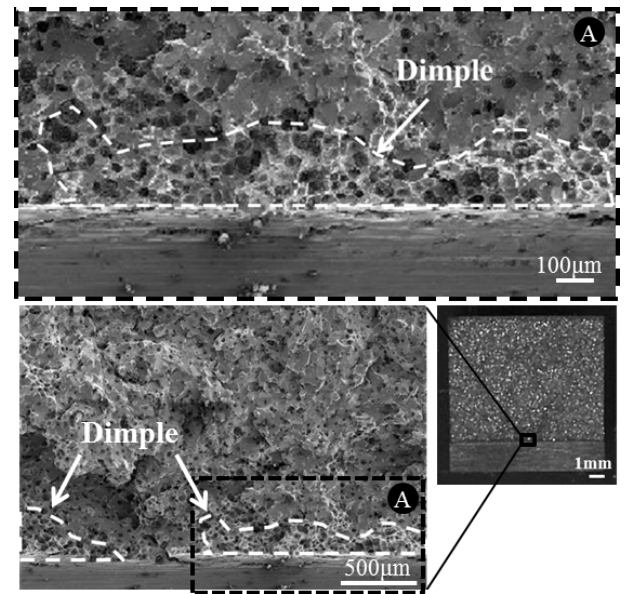


Fig. 11 SEM images of the notch root area in Fig. 7(d).

that brittle fracture occurs just after forming the slight dimple ductile fracture at the notch root. In this experiment at $T = 22^\circ\text{C}$, the dimple pattern is always observed at every notch root. Hence, $\sigma_{b,max}$ keeps increasing with increasing $\dot{\epsilon}$ as far as the fracture origin is ductile. We believe that $\sigma_{b,max}$ could be a significant criterion for designing various components.

3.2 Dependency of absorbed energy and notch bending strength on strain rate at -20°C for 4% Si ductile cast iron

Figure 12 shows the load-displacement curves at lower temperature $T = -20^\circ\text{C}$ for 4% Si iron. Different from the test results at $T = 22^\circ\text{C}$, the maximum load P_{max} decreases at higher strain rate $\dot{\epsilon}$, and almost no crack propagation energy E_p is recognized at every strain rate. Therefore, the total absorbed energy E_t becomes almost same as E_i , the crack initiation energy, as given in Fig. 13(a). E_i starts dropping at $\dot{\epsilon}_{i-4\%Si} = 0.11 \times 10^{-2}$, as indicated by the black arrow. Above this critical strain rate $\dot{\epsilon}_i$, E_i linearly decreases with the increase in $\dot{\epsilon}$.

Figure 14 shows SEM images of fracture surface near the

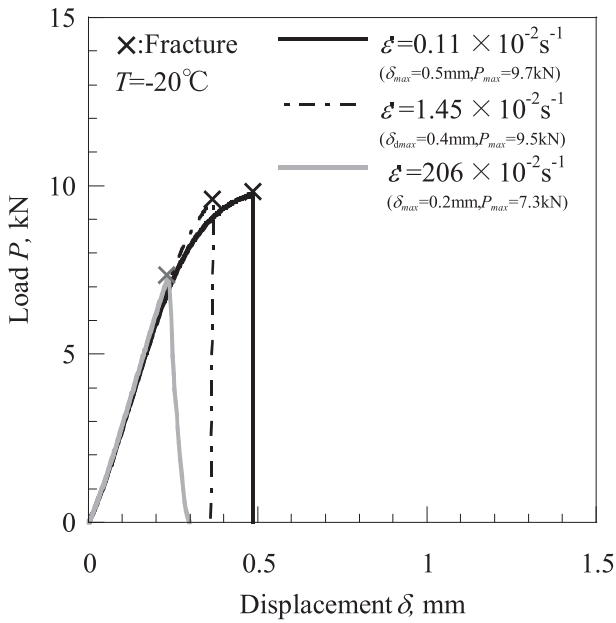


Fig. 12 Load-displacement curves tested under various $\dot{\epsilon}$ at $T = -20^\circ\text{C}$ for 4%Si iron.

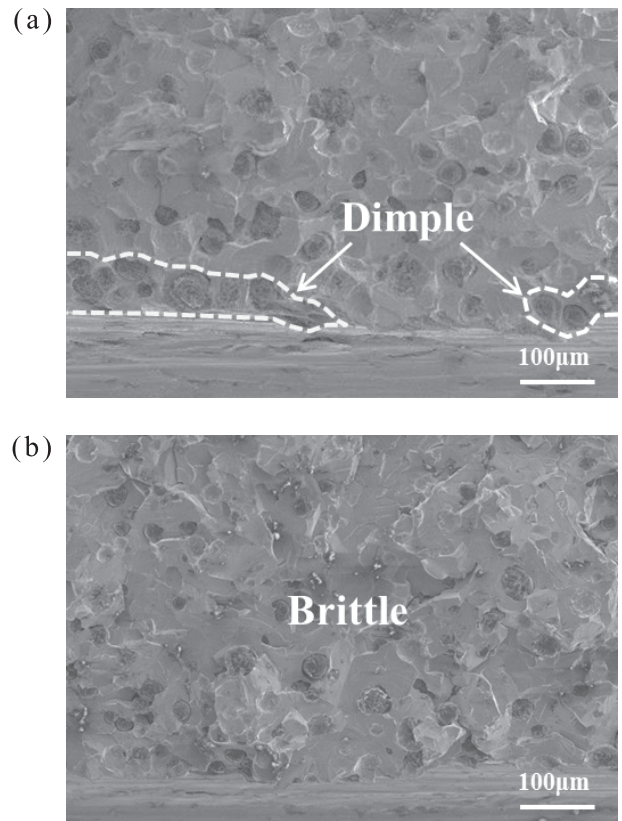


Fig. 14 SEM image of the notch root area on fracture surface of specimen tested at -20°C , $\dot{\epsilon} = 0.11 \times 10^{-2} \text{ s}^{-1}$ (a), $\dot{\epsilon} = 1.45 \times 10^{-2} \text{ s}^{-1}$ (b) in Fig. 12.

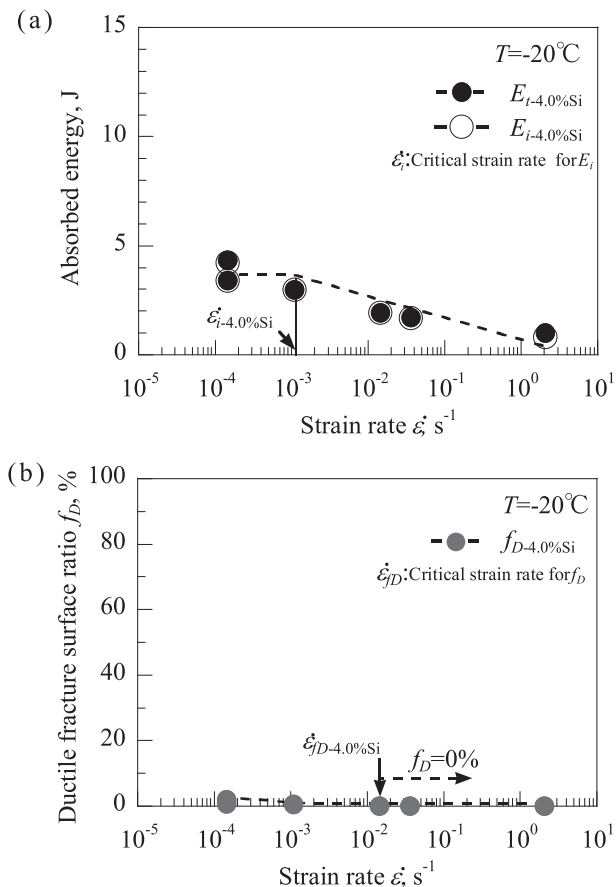


Fig. 13 Influence of $\dot{\epsilon}$ on E_r , E_i (a) and f_D (b) at $T = -20^\circ\text{C}$ for 4%Si iron.

notch root. A very small amount of dimple patterns are observed on the specimen broken at strain rate of $0.11 \times 10^{-2} \text{ s}^{-1}$, while no dimple appears at $1.45 \times 10^{-2} \text{ s}^{-1}$. The critical strain rate for null ductile fracture surface ratio $\dot{\epsilon}_{fD}$ is determined as $\dot{\epsilon}_{fD-4\%Si} = 1.45 \times 10^{-2} \text{ s}^{-1}$ as shown in Fig. 13(b).

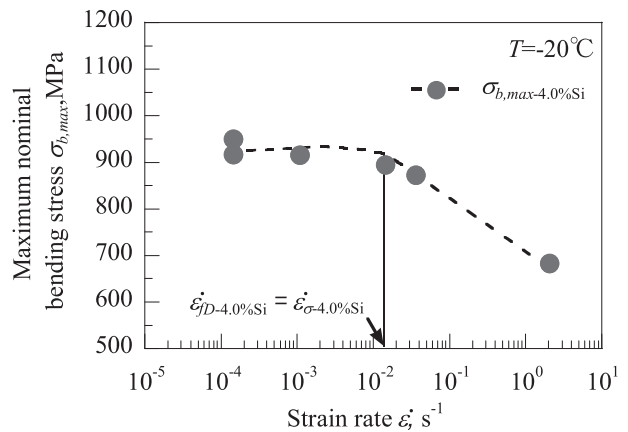


Fig. 15 Influence of $\dot{\epsilon}$ on $\sigma_{b,max}$ at $T = -20^\circ\text{C}$ for 4%Si iron.

Figure 15 shows the relationship between the maximum nominal bending stress $\sigma_{b,max}$ and $\dot{\epsilon}$. The $\sigma_{b,max}$ value keeps 900 MPa at lower $\dot{\epsilon}$, almost the same value as $\sigma_{b,max}$ obtained at $T = 22^\circ\text{C}$, then it starts decreasing at $\dot{\epsilon}_{\sigma-4\%Si} = 1.45 \times 10^{-2} \text{ s}^{-1}$. This critical $\dot{\epsilon}_{\sigma-4\%Si}$ coincides with $\dot{\epsilon}_{fD-4\%Si}$, indicating that $\dot{\epsilon}_\sigma$ closely related to the presence of dimple pattern at notch root.

3.3 Influence of silicon content on critical strain rate for absorbed energy and notch bending strength

Figure 16 shows the influence of $\dot{\epsilon}$ on E_t , E_i and $\sigma_{b,max}$ at $T = 22^\circ\text{C}$ for 3.3~3.7%Si iron. In Fig. 16(a), $E_{t-3.7\%Si}$ starts dropping at $\dot{\epsilon}_{p-3.7\%Si} = 2.5 \times 10^{-1} \text{ s}^{-1}$. This critical strain rate

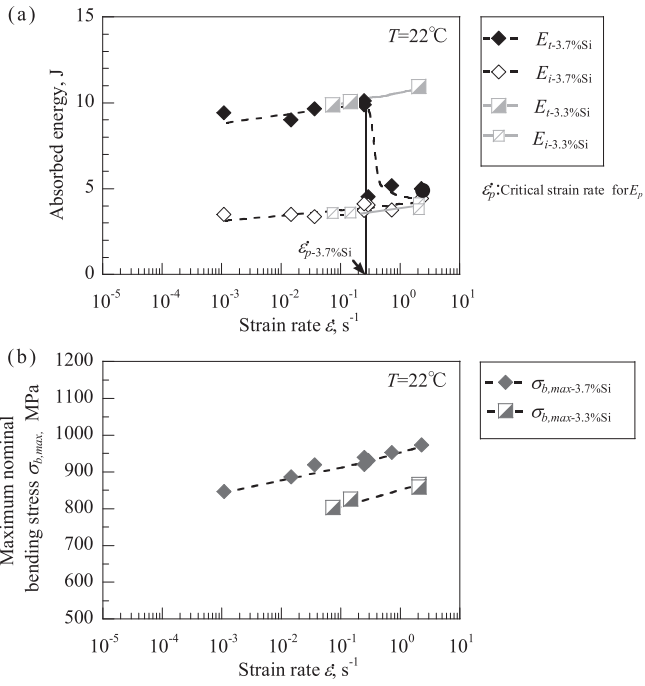


Fig. 16 Influence of $\dot{\epsilon}$ on E_t , E_i (a) and $\sigma_{b,max}$ (b) at $T=22^{\circ}\text{C}$ for 3.3~3.7%Si iron.

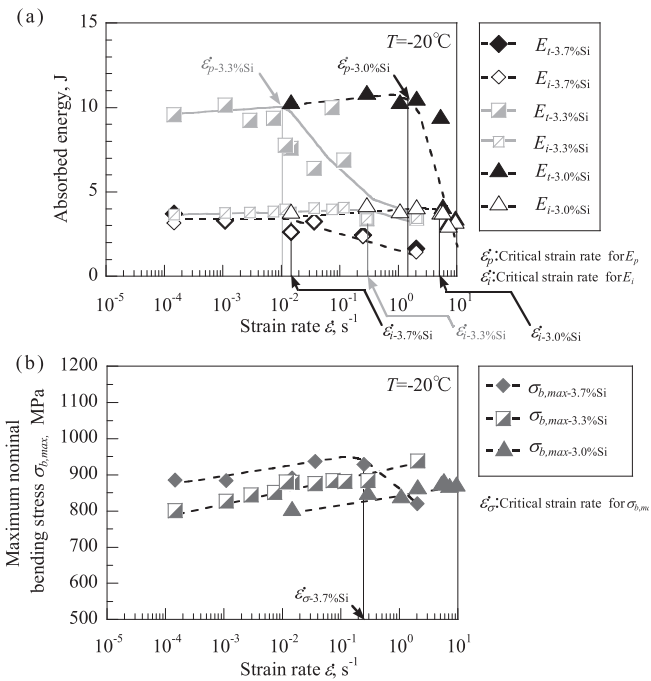


Fig. 17 Influence of $\dot{\epsilon}$ on E_t , E_i (a) and $\sigma_{b,max}$ (b) at $T=-20^{\circ}\text{C}$ for 3~3.7%Si iron.

$\dot{\epsilon}_p$ of 3.7%Si iron is higher than that of 4%Si iron in Fig. 9. $E_{t-3.3\%Si}$ keeps increasing in the experiment strain range. Figure 17 shows the influence of $\dot{\epsilon}$ on E_t , E_i and $\sigma_{b,max}$ at $T=-20^{\circ}\text{C}$ for 3.0~3.7%Si iron. $E_{i-3.7\%Si}$ and $\sigma_{b,max-3.7\%Si}$ start decreasing at $\dot{\epsilon}_i = 1.5 \times 10^{-2} \text{ s}^{-1}$ and at $\dot{\epsilon}_{\sigma-3.7\%Si} = 2.5 \times 10^{-1} \text{ s}^{-1}$, respectively. These critical strain rates are also higher than those of 4%Si iron in Figs. 13 and 15. These figures show every critical strain rate becomes higher with decreasing silicon content.

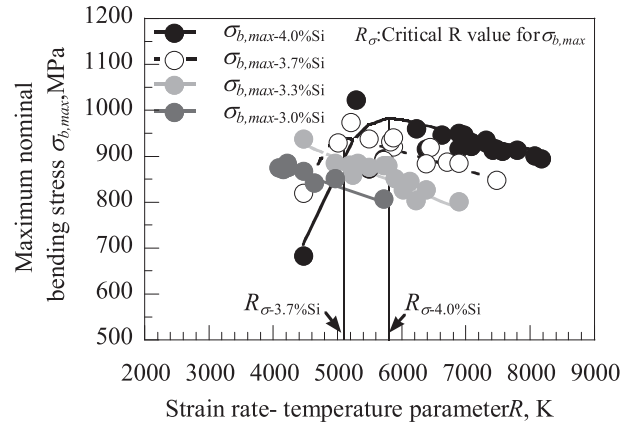


Fig. 18 Relationships between R value and $\sigma_{b,max}$ for 3~4%Si irons.

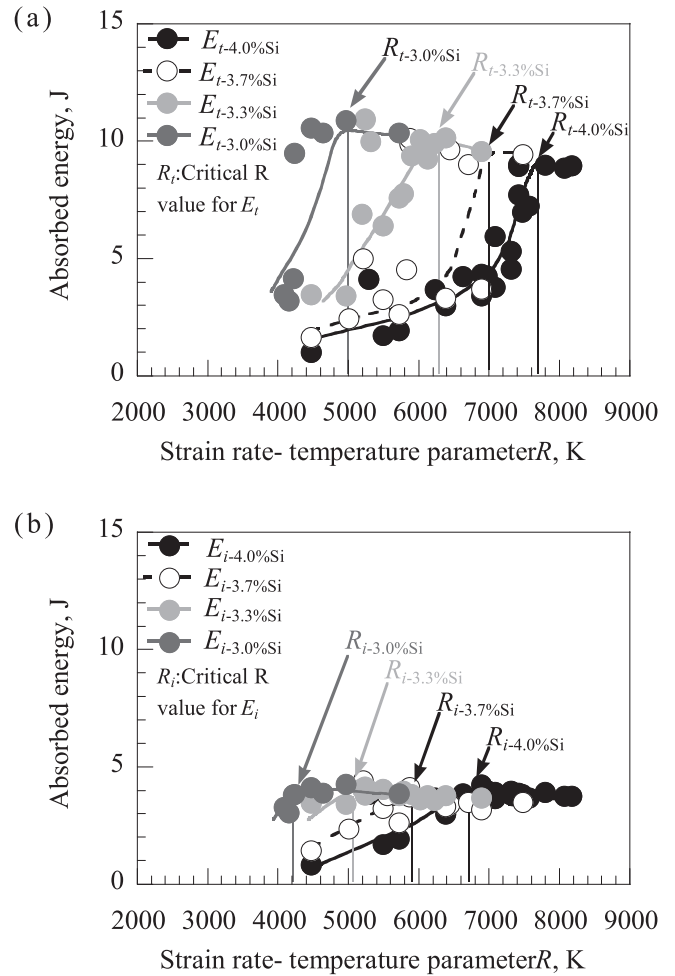


Fig. 19 Relationships between R value and E_t (a), E_i (b) for 3~4%Si irons.

3.4 Application of strain rate-temperature parameter to the evaluation of strength and toughness

Based on Bennett and Sinclair's theory on the effects of $\ln \dot{\epsilon}$ and $1/T$ on yield phenomena of steel and BCC metals²⁴⁾, the strain rate-temperature parameter R , given by eq. (3), has been introduced to explain the influence of $\dot{\epsilon}$ and T on the tensile strength as well as yield stress of steel²⁵⁻²⁷⁾, where $T = \text{temperature}$, $A = 10^8 \text{ s}^{-1}$ ²⁴⁾, $\dot{\epsilon} = \text{strain rate}$.

$$R = T \ln(A/\dot{\epsilon}) \quad (3)$$

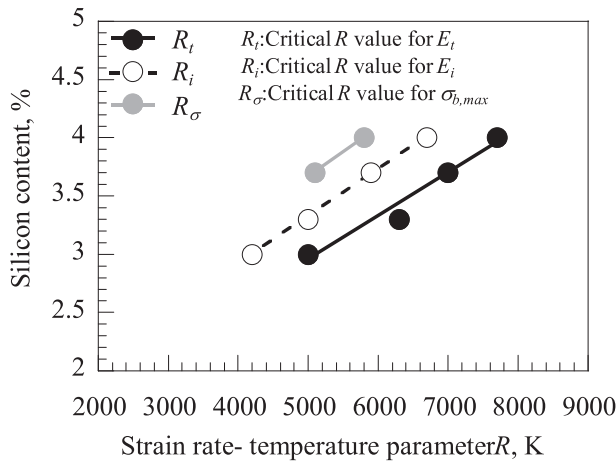


Fig. 20 Relationships between critical R value and Si content for 3~4%Si irons.

A good correlation between notch tensile strength and R value was also reported on ductile cast iron²⁸). Therefore, we tried to correlate our experimental data of $\sigma_{b,max}$ to R value.

As shown in Fig. 18, there is a good correlation between $\sigma_{b,max}$ and R value for each Si irons. $\sigma_{b,max}$ tends to increase linearly with the decrease in R value. Here, decreasing R means increasing $\dot{\epsilon}$ or decreasing T , or both. This result is consistent with previous research reports on steels and ductile cast iron^{27,28}). However, $\sigma_{b,max}$ becomes smaller below the critical value R_σ for 3.7 and 4%Si irons, because completely brittle fracture occurs below R_σ . R_σ becomes lower with decreasing silicon content, as indicated in Fig. 18.

As the higher strain rate and the lower temperature give similar effects on the toughness of steel and ductile cast iron^{9,29}), we tried to correlate our experimental data of absorbed energy E_t and E_i to R value. Figure 19 shows the relationship between absorbed energy and R for each Si irons. Although there are some scatters, good correlations are recognized for each Si iron, and the critical R values, R_t and R_i , become lower with the decreasing of silicon content. Based on Figs. 18 and 19, Fig. 20 shows the relationships between each critical R value and silicon content. R_t , R_i and R_σ decrease linearly with decreasing the silicon content. In addition, the critical value is lower in the order of R_σ , R_i and R_t . Based on this figure, we can estimate the appropriate silicon content of ductile cast iron components, considering the lowest service temperature and the highest strain rate applied on the part.

4. Conclusions

Using Charpy V-notch specimens, dynamic three-point bending tests are conducted on 3~4%Si ferritic ductile cast iron at stroke speed of 10^{-3} ~ 10^2 mm/s, and at -20 ~ 22°C . The notch bending strength as well as the absorbed energy in fracture process is determined, and the results are discussed with the strain rate-temperature parameter R . The following conclusions are obtained.

(1) Based on load-displacement curves, the crack initiation energy E_i , the crack propagation energy E_p , the total absorbed energy E_t and the maximum nominal bending stress $\sigma_{b,max}$ are

defined and displayed in relation to the strain rate $\dot{\epsilon}$.

(2) E_p and E_t of 3.7% and 4.0%Si iron start dropping at $\dot{\epsilon}_p = 2.5 \times 10^{-1} \text{ s}^{-1}$ and $1.3 \times 10^{-3} \text{ s}^{-1}$, while the crack initiation energy E_i is almost unchanged even above these critical strain rate $\dot{\epsilon}_p$ at 22°C .

(3) At -20°C , E_i and maximum nominal bending stress $\sigma_{b,max}$ start dropping at their specific critical strain rate. The critical strain rate of E_i is lower than that of $\sigma_{b,max}$.

(4) $\sigma_{b,max}$ keeps increasing with increasing $\dot{\epsilon}$ as far as the dimple patterns appear at notch root.

(5) The higher strain rate and the lower temperature give similar effects on the strength and toughness of high silicon ductile cast iron. $\sigma_{b,max}$, E_t and E_i of each Si iron is well expressed in relation to strain rate-temperature parameter R , $T \ln(A/\dot{\epsilon})$.

(6) The critical R values for E_t , E_i and $\sigma_{b,max}$ (R_t , R_i and R_σ) decrease linearly with decreasing the silicon content of iron. The critical value is lower in the order of R_σ , R_i and R_t , indicating R_σ gives a wider design tolerance.

REFERENCES

- 1) R. Larker: China Foundry **6** (2009) 343–351.
- 2) R. Larker: *Proc. NEWCAST Forum*, (Bundesverband der Deutschen Gießerei Industrie, 2011), p.29.
- 3) H. Löblich: *Proc. Deutscher Gießereitag 2013 und 5. NEWCAST Forum*, (Verein Deutscher Giessereifachleute, 2013), pp.14–17.
- 4) EN 1563: *Founding-Spheroidal graphite cast irons*, 2011.
- 5) T. Umetani, T. Ikeda, N. Sura, K. Ashizuka, T. Nemoto, H. Takada and K. Ogi: J.JFS. **86** (2014) 36–42.
- 6) T. Okumoto and T. Aizawa: Imono **35** (1963) 670–677.
- 7) K. Nagai, K. Kishitake and T. Owadano: Imono **58** (1986) 350–355.
- 8) H. Nagayoshi, H. Yasuda and K. Imanishi: J.JFS. **68** (1996) 506–511.
- 9) H. Yamamoto, T. Kobayashi and H. Fujita: J.JFS. **72** (2000) 107–112.
- 10) K. Nagai, S. Izumi, K. Kishitake and T. Owadano: Imono **58** (1986) 653–658.
- 11) JIS-G5502: *Spheroidal graphite iron castings*, 2001.
- 12) JIS- G 0551: *Steels-Micrographic determination of the apparent grain size*, 2005.
- 13) JIS-Z 2243 standard: *Brinell hardness test-Test method*, 2008.
- 14) JIS-Z2241: *Metallic materials-Tensile testing-Method of test at room temperature*, 2011.
- 15) T. Shiota, T. Matuoka and S. Komatu: Imono **63** (1991) 601–606.
- 16) JIS-Z2242: *Method for Charpy pendulum impact test of metallic materials*, 2005.
- 17) R. Sandstrom and Y. Bergstrom: *Met. Sci.* **18** (1984) 177–186.
- 18) N. Sugiura, T. Kobayashi, I. Yamamoto, S. Nishido and K. Hayashi: *J. Jpn. Inst. Light Met.* **45** (1995) 638–642.
- 19) K. Matsugi, G. Bando, G. Sasaki and O. Yanagisawa: J.JFS. **79** (2007) 229–234.
- 20) T. Kobayashi, H. Matsubara and Y. Ueda: Tetsu-to-Hagane **69** (1983) 1183–1188.
- 21) S. Nunomura and M. Nakashiro: Tetsu-to-Hagane **64** (1978) 860–869.
- 22) T. Nobuki, T. Shiota and M. Hatate: J.JFS. **75** (2003) 749–756.
- 23) T. Nobuki, T. Shiota and M. Hatate: J.JFS. **76** (2004) 555–561.
- 24) P.E. Bennett and G.M. Sinclair: *Trans. ASME* **65** (1966) 518–524.
- 25) E. Fuji, Y. Ohkuma, Y. Kawaguchi and M. Tsukamoto: *The society of naval architects of Japan* **158** (1985) 619–629.
- 26) K. Goto, H. Hirose and M. Toyoshada: *The society of naval architects of Japan* **176** (1994) 501–507.
- 27) F. Minami, T. Hashida, M. Toyoda, J. Morikawa, T. Ohmura, K. Arimochi and N. Konda: *The society of naval architects of Japan* **184** (1998) 453–463.
- 28) H. Yamamoto, T. Kobayashi and H. Fujita: Tetsu-to-Hagane **85** (1999) 765–770.
- 29) M. Toyosada, E. Fujii, K. Nohara, Y. Kawaguchi, K. Arimochi and K. Isaka: *The society of naval architects of Japan* **161** (1997) 343–356.